Dalton Transactions

ROYAL SOCIETY OF CHEMISTRY

PAPER

View Article Online
View Journal | View Issue

Cite this: *Dalton Trans.*, 2024, **53**, 8177

Three-dimensional bimodal pore-rich G/MXene sponge amalgamated with vanadium diselenide nanosheets as a high-performance electrode for electrochemical water-oxidation/reduction reactions†

Khadija Chaudhary, [a] Sonia Zulfiqar, [b,c] Zeid A. ALOthman, [d] Imran Shakir, [d] Muhammad Farooq Warsi *[a] and Eric W. Cochran *[c]

Received 28th February 2024,
Accepted 16th April 2024

DOI: 10.1039/d4dt00602j

rsc.li/dalton

Exploring new strategies to design non-precious and efficient electrocatalysts can provide a solution for sluggish electrocatalytic kinetics and sustainable hydrogen energy. Transition metal selenides are potential contenders for bifunctional electrocatalysis owing to their unique layered structure, low band gap, and high intrinsic activities. However, insufficient access to active sites, lethargic water dissociation, and structural degradation of active materials during electrochemical reactions limit their activities, especially in alkaline media. In this article, we report a useful strategy to assemble vanadium diselenide (VSe_2) into a 3D MXene/rGO-based sponge-like architecture (VSe_2@G/MXe) using hydrothermal and freeze-drying approaches. The 3D hierarchical meso/macro-pore rich sponge-like morphology not only prevents aggregation of VSe_2 nanosheets but also offers a kinetics-favorable framework and high robustness to the electrocatalyst. Synergistic coupling of VSe_2 and a MXene/rGO matrix yields a heterostructure with a large specific surface area, high conductivity, and multi-dimensional anisotropic pore channels for uninterrupted mass transport and gas diffusion. Consequently, VSe_2@G/MXe presented superior electrochemical activity for both the HER and OER compared to its counterparts (VSe_2 and VSe_2@G), in alkaline media. The overpotentials required to reach a cathodic and anodic current density of 10 mA cm^{-2} were 153 mV (Tafel slope = 84 mV dec^{-1}) and 241 mV (Tafel slope = 87 mV dec^{-1}), respectively. The R_{ct} values at the open circuit voltage were as low as 9.1 Ω and 1.41 Ω for the HER and OER activity, respectively. Importantly, VSe_2@G/MXe withstands a steady current output for a long 24 h operating time. Hence, this work presents a rational design for 3D microstructures with optimum characteristics for efficient bifunctional alkaline water-splitting.

1. Introduction

The global energy crisis, as a consequence of the shortage of fossil fuel reserves and the increase in fuel costs, is one of the most prevailing issues affecting various sectors of the world's economies.[1–3] In addition, global campaigns against CO_2 emission are putting pressure on different countries to limit their use of fossil fuels to combat climate change.[4,5] Consequently, the issue of energy security should be at the forefront of each country's policy for a secure and self-sufficient future. For this, we need alternative, low-cost, clean energy resources. In this context, hydrogen fuel is a clean and efficient source of energy because of its high gravimetric energy density and non-harmful by-product (*i.e.*, H_2O). Though hydrogen is considered a green fuel, 95% of the

---

[a] *Institute of Chemistry, Baghdad-ul-Jadeed Campus, The Islamia University of Bahawalpur, Bahawalpur, 63100, Pakistan. E-mail: farooq.warsi@iub.edu.pk*

[b] *Department of Chemistry, Faculty of Science, University of Ostrava, 30. Dubna 22, Ostrava 701 03, Czech Republic*

[c] *Department of Chemical and Biological Engineering, Iowa State University, Sweeney Hall, 618 Bissell Road, Ames, Iowa 50011, USA. E-mail: ecochran@iastate.edu*

[d] *Department of Chemistry, College of Science, King Saud University, P. O. Box 2455, Riyadh 11451, Saudi Arabia*

† Electronic supplementary information (ESI) available: EDX spectra of (a) VSe_2, (b) VSe_2@G, and (c) VSe_2@G/MXe (Fig. S1), XRD patterns of MXene and rGO (Fig. S2), *I–V* profiles of VSe_2, VSe_2@G, and VSe_2@G/MXe (Fig. S3), LSV curve of G/MXe for the HER (Fig. S4), LSV curve of G/MXe for the OER (Fig. S5), C_{dl} results for VSe_2, VSe_2@G, and VSe_2@G/MXe (Fig. S6), ECAS-normalized LSV curves of VSe_2 and VSe_2@G/MXe for the HER (Fig. S7), ECAS-normalized LSV curves of VSe_2 and VSe_2@G/MXe for the OER (Fig. S8), comparison of the HER performance of VSe_2@G/MXe with that of similar reported electrocatalytic materials (Table S1), and comparison of the OER performance of VSe_2@G/MXe with that of similar reported electrocatalytic materials (Table S2). See DOI: https://doi.org/10.1039/d4dt00602j

production of hydrogen fuel itself consumes carbon-based raw materials, mostly coming from fossil fuels.[6,7] On the other hand, the production of hydrogen from water electrolysis through the hydrogen evolution reaction (HER) includes the CO_2 neutral reactant.[8] Besides, the second half reaction during water electrolysis, *i.e.*, oxygen evolution reaction (OER), results in the formation of the by-product oxygen which is an important industrial gas and finds applications in combustion, semiconductor production, and wastewater treatment.[9,10] The state-of-the-art electrocatalysts applied in water electrolysers are RuO_2, IrO_2, and Pt.[11] Due to the scarcity and high prices of these noble metal-based electrocatalysts, hydrogen production from water electrolysis is accompanied by high production costs that hinder its market penetration. In this regard, several attempts have been made in recent years to design inexpensive Earth-abundant transition metal based electrocatalysts for the HER, OER, and overall water-splitting.

Driven by their high electrical conductivity and redox activity, transition metal selenides (TMSes) such as $NiSe_2$,[12] $Ni_{0.85}Se$,[13] Co_3Se_4,[14] $FeSe_2$,[15] MoSe,[16] and Cu_2Se[17] have been widely explored for water-splitting applications. The selenium atom in TMSes may bind with other metal atoms due to the close energy level of the 3d orbital with those of 3s and 3p.[18] This unique electronic structure induces an enhanced metallic characteristic in TMSes that is beneficial for electron transport and the occurrence of redox reactions.[19] Apart from the above-mentioned TMSe electrocatalysts, 2D vanadium diselenide (VSe_2) with a group-five transition metal (with an enhanced metallic characteristic) shows a very high electrical conductivity (~1000 S m^{-1} at 300 K).[20] Considering the inherent electrochemistry intrinsic to transition metal (V) and chalcogen (Se), VSe_2 has been predicted to have strong potential for electrochemical applications.[21] In addition, the unique 2D layered chalcogenide-like (MX_2, M = metal and X = S, Se, and Te) structure of VSe_2 can offer it high concentration of active sites desirable for efficient catalytic activity.[22] Lately, VSe_2 nanosheets prepared by the colloidal route showed impressive HER activity with a very low overpotential of 206 mV at a current density of 10 mA cm^{-2}.[23] In a similar report, Yan and co-workers reported sufficient potential of VSe_2 nanosheets for HER activity.[24] Most recently, Liu *et al.* studied the efficiency of hydrothermally synthesized layered VSe_2 for overall water splitting.[25] The as-synthesized electrocatalyst revealed an optimal electrocatalytic potential for the HER and OER activity with overpotentials of 1.011 V and 2.467 V at 10 mA cm^{-2}, respectively. However, the problem with 2D layered structures is the interlayer interactions that stimulate restacking among layers and conceal the active sites.[26] Furthermore, a high electron density of unoccupied d-orbitals of vanadium in VSe_2 suggests a high Gibbs free energy (ΔG_H) for hydrogen adsorption (large Heyrovsky and Tafel steps), which leads to sluggish reaction kinetics.[20] Constructing heterostructures of TMSes with carbon materials can be a useful approach to overcome the stacking issues. The synergistic interactions among the pristine TMSe and second phase optimize ΔG_H for hydrogen adsorption, thus facilitating the catalytic process.[27]

MXenes ($M_{n+1}X_nT_x$, M = transition metal, X_n = C and N, and T_x = surface terminal groups) are a new family of 2D transition metal carbides, nitrides, or carbonitrides that have promising potential to be used as hybridizing matrices.[28] MXenes possess high metallic conductivity and hydrophilicity that are seldom realized by other hybridizing materials.[29] Reports on MXene composites such as CoS–MXene,[30] FeS_2–MXene,[31] CuS–Cl terminated MXene,[32] $CoSe_2$@MXene,[33] and $NiCo_2Se_4$–MXene[34] have shown significant improvement in the electrocatalytic activity. Recently, the focus has been shifted to designing 3D architectures of MXenes (hydrogel, foams, and sponges).[35,36] Despite many recent reports on 3D MXenes, their composite systems still need to be explored. To the best of our knowledge, the combination of 2D layered MX_2 with a 3D MXene system has not yet been reported.

In view of the above discussion, herein, we report a novel electrocatalyst (VSe_2@G/MXe) where 2D VSe_2 nanosheets are assembled into a $Ti_3C_2T_x$ MXene (hereafter represented as MXene) based 3D sponge. Due to the stiff nature of MXene sheets, graphene oxide (GO) is used as a gelation agent to construct a 3D MXene sponge (henceforth represented as G/MXe). The 3D VSe_2@G/MXe sponge-like hybrid exhibits outstanding performance towards both the HER and OER. rGO not only served as the gelation agent to assemble the VSe_2@G/MXe monolith but also provided a high specific surface area to the electrocatalyst. The high conductivity of the MXene combined with rGO provided fast charge transport. The active sites of VSe_2 amalgamated into the highly porous G/MXe sponge were easily accessible to the electrolyte for electrochemical activity. Intriguingly, VSe_2@G/MXe exhibited a significant improvement in the overpotential for the HER (153 mV@10 mA cm^{-2}) and the OER (241 mV@10 mA cm^{-2}) compared with VSe_2 and VSe_2@G. Consequently, this study provides insight into the development of MXene-based 3D composite materials as a useful strategy to improve the energy conversion performance of electrocatalysts.

2. Experimental section

2.1. Chemicals

Ammonium metavanadate (NH_4VO_3; 99.99%), selenium dioxide (SeO_2; 999.99%), formic acid (HCOOH; ≥99%), MAX powder (Ti_3AlC_2; ≥90%, ≤200 μm particle size), and hydrofluoric acid (HF; 40%) were purchased from Sigma Aldrich. All chemicals were used as procured. Nickel foam (NF; 150 × 150 mm and thickness 1.6 mm) from Sigma Aldrich was used as a substrate to prepare electrodes. Distilled water from a self-regulating plant was used throughout the experimental work.

2.2. Synthesis of vanadium diselenide (VSe_2)

For the synthesis of VSe_2, NH_4VO_3 (118.4 mg) and SeO_2 (220.9 mg) were added to 40 mL of distilled water and stirred for 5 min. 5 mL of HCOOH was added to the above stirring solution in a dropwise manner, and the mixture was allowed to stir for further 5 min. Next, the solution was transferred to a

50 mL autoclave and incubated at 220 °C for 24 h. After completion of the reaction, the autoclave was naturally cooled down and precipitates were separated through ultracentrifugation. The precipitates were washed with ethanol and water to remove unreacted salts and dried at 60 °C overnight to obtain VSe_2 powder. The formation of VSe_2 from the precursors can be represented by the following eqn (1)–(3):[25]

$$VO^{-3} + HCOOH + 2H^{+} \rightarrow VO^{+2} + CO_2 + 2H_2O \quad (1)$$

$$SeO_2 + HCOOH + 2H^{+} \rightarrow H_2Se + CO_2 + 2H_2O \quad (2)$$

$$VO^{+2} + 2H_2Se \rightarrow VSe_2 + 2H^{+} + H_2O \quad (3)$$

2.3. Synthesis of VSe_2@G/MXe

For the synthesis of VSe_2@G/MXe, first, GO and MXene were prepared. Synthesis of GO was carried out by the Hummers method reported elsewhere.[37] To synthesize MXene, 1 g of MAX powder was slowly added to 20 mL of HF solution with continuous stirring. The reaction mixture was left to stir at room temperature for 48 h. Next, the HF-etched MXene was washed with distilled water to neutralize MXene particles. Exfoliation of the MXene was carried out in distilled water under ultrasonication conditions. Finally, the MXene was dried at 60 °C to obtain MXene powder. Next, a suspension of VSe_2 was ultrasonically prepared by dispersing VSe_2 (20 mg) in 10 mL of distilled water. A second suspension of GO : MXene (20 : 10 mg) was also prepared ultrasonically in 10 mL of distilled water. VSe_2 suspension prepared during the first step was added to the GO : MXene suspension and the mixture was further treated under ultrasonication conditions for 30 min to obtain a homogeneous solution. Next, 20 mg of ascorbic acid was added to the obtained suspension, and the mixture was processed hydrothermally at 70 °C for 4 h. The as-obtained monolith was freeze-dried at −90 °C to obtain VSe_2@G/MXe. For comparison, VSe_2@G was also prepared by following the same procedure without the addition of the MXene.

2.4. Characterization

A LabX XRD-6100 diffractometer (CuKα, λ = 0.154 nm) was used to elucidate the crystalline structure and composition of the prepared materials. FT-IR spectra were recorded on a Shimadzu FT-IR affinity/1S. The morphology was recorded using a ZEISS LEO SUPRA 55 field emission scanning electron microscope. A JEOL JCM-6000 Plus SEM instrument was used to collect the elemental data. A Micromeritics ASAP 2020 physisorption analyzer was used to determine the surface properties of electrocatalysts. A Keithley voltage source 6487/E was used to investigate the electrical behavior. The electrochemical water-splitting application study was carried out on a GAMRY Potentiostat interface 5000/E.

2.5. Water-splitting measurements

For electrochemical water-splitting, a slurry was prepared from the synthesized electrocatalysts. 10 mg of each electrocatalyst (VSe_2, VSe_2@G, and VSe_2@G/MXe) was mixed with Nafion binder and ethanol and ultrasonicated for 5 min. The slurry was deposited on Ni foam (fixed area = 1 × 1 cm^2) and dried at room temperature. The prepared electrodes were used as working electrodes in a three-electrode workstation. Platinum wire and silver/silver chloride were applied as the auxiliary and reference electrodes, respectively. 1 M KOH was used as the electrolyte medium to collect linear sweep voltammetry (LSV), cyclic voltammetry (CV), impedance, and chronoamperometry data. LSV and CV curves were recorded at 3 mV s^{-1} and 20–120 mV s^{-1}, respectively. Impedance or EIS measurements were conducted at an AC voltage of 5 mV with initial and final frequencies of 0.1 Hz and 100 kHz, respectively. Chronoamperometry stability tests for the HER and the OER were performed for 24 h at a fixed potential. In addition, all the potential (E) values were referenced to the reversible hydrogen electrode (RHE) using the following eqn (4):

$$E(\mathrm{RHE}) = E(\mathrm{Ag/AgCl}) + 0.197 + (0.0591 \times \mathrm{pH}) \quad (4)$$

3. Results and discussion

3.1. Microstructure assembly and morphological and compositional analyses

Fig. 1 schematically illustrates the synthesis of the VSe_2@G/MXe microstructure. For hydrothermal assembly, the $Ti_3C_2T_x$ MXene was obtained through acidic etching of the Al layer from Ti_3AlC_2 MAX powder. First, the MXene suspension was treated with GO ultrasonically in the presence of the hydrothermally synthesized VSe_2. Due to the surface-terminated polar groups, MXene sheets get attracted and stick to the surface of GO sheets. Next, when the ultrasonically treated homogeneous suspension was treated under the hydrothermal conditions in the presence of ascorbic acid, it resulted in the generation of π–π interactions leading to the hydrophobic effect among the macroscopic rGO sheets. As the hydrophobic interactions dominate the hydrophilic interactions at the rGO interface, the partially reduced rGO with attached MXene sheets undertook phase separation into a 3D monolith that is then freeze-dried into a cross-linked porous microstructure.

FESEM analysis was used for a comprehensive structural and morphological study of the prepared electrocatalysts. The HF-etched MXene in Fig. 2(a) shows a few-layer accordion-like structure with an obvious interlayer spacing, whereas the FESEM image of bare VSe_2, shown in Fig. 2(b), shows the existence of thin VSe_2 nanosheets that stack on each other to form quasi-lamellar structures with a relatively smooth surface. FESEM images in Fig. 2(d–f) and (g–i) display different sectional views of VSe_2@G and VSe_2@G/MXe microstructures, respectively. A pore-rich 3D sponge-like structure can be observed for VSe_2@G and VSe_2@G/MXe. Fig. 2(d and g) shows the preferred direction of growth of ice crystals for the prepared microstructures. Certainly, during the freeze-drying process, cross-linked walls of VSe_2@G and VSe_2@G/MXe monoliths under the action of the ice template are repelled by the growing ice crystals leading to the accumulation of cell

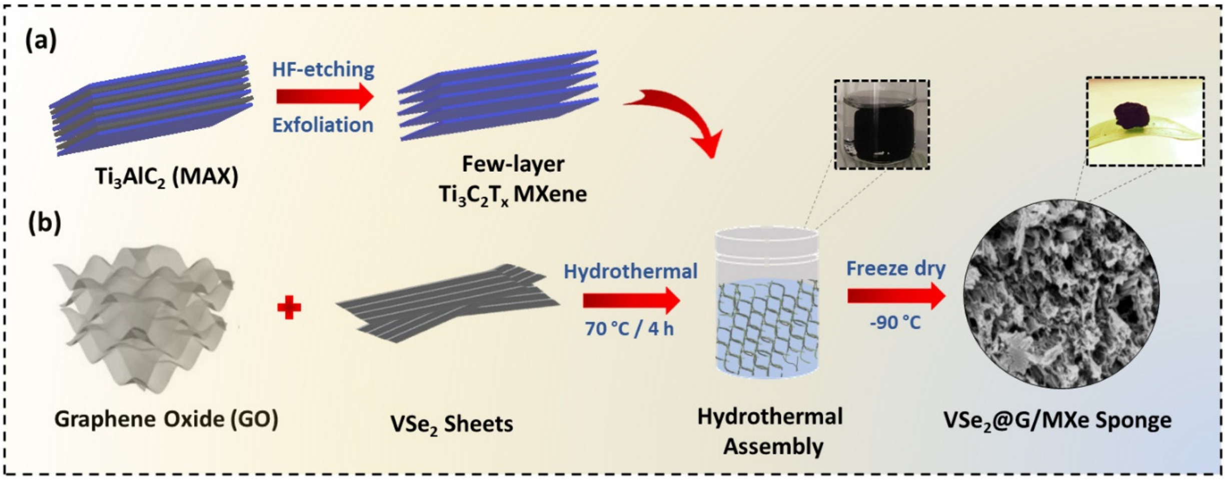

Fig. 1 Schematic illustrations of (a) HF-etching of the MAX phase and (b) hydrothermal assembly of VSe_2, MXene, and rGO into VSe_2@G/MXe.

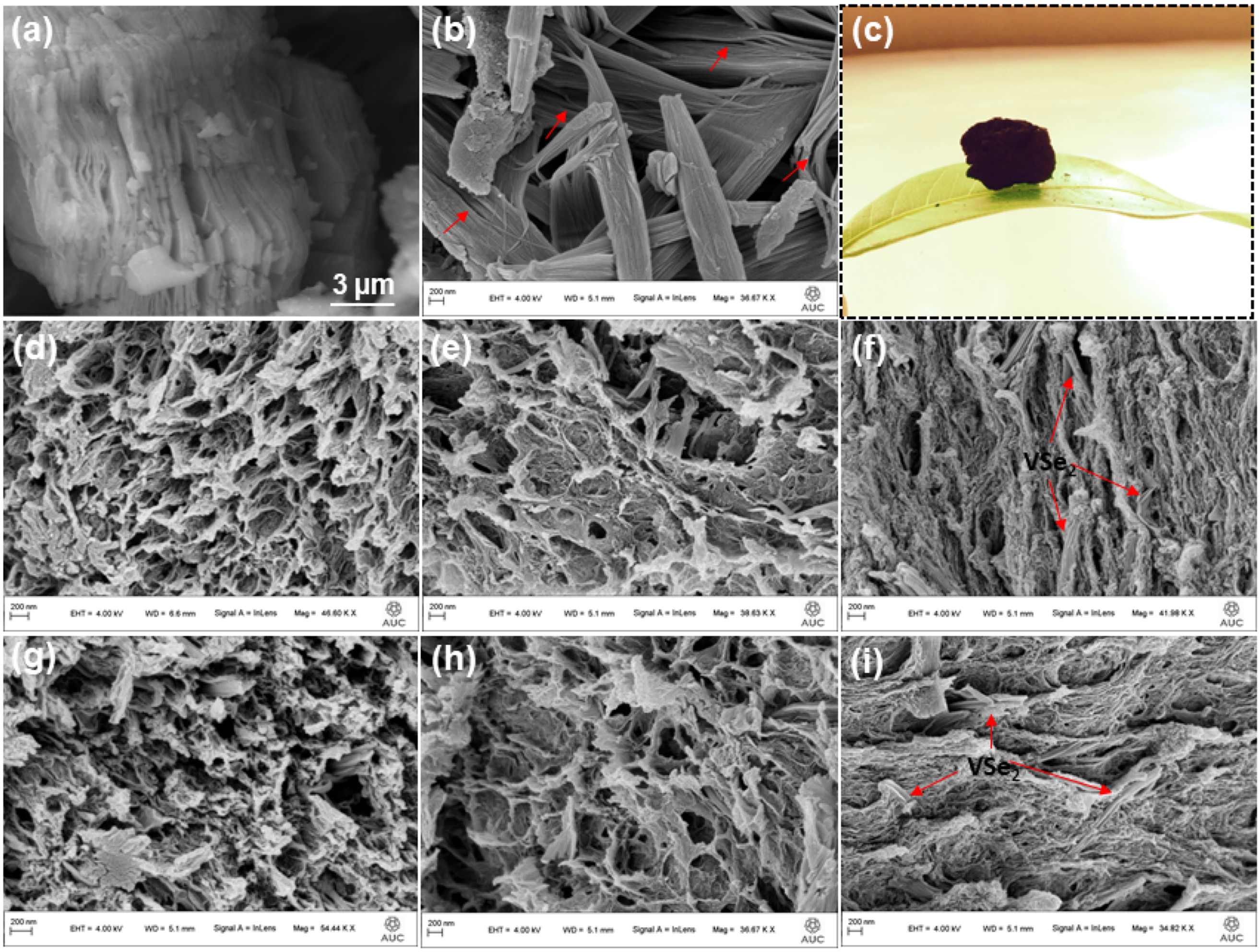

Fig. 2 FESEM images of (a) MXene and (b) VSe_2 nanosheets, and (c) photograph of VSe_2@G/MXe on a leaf; different sectional view images of (d–f) VSe_2@G and (g–i) VSe_2@G/MXe.

walls parallel to the ice template.[38] The cross-section views in Fig. 2(e and h) confirm that the pores generated as a result of the cross-linking and the ice-templating effect cumulate in anisotropic porous channels within VSe_2@G and VSe_2@G/MXe. Meanwhile, VSe_2 nanosheets simultaneously intervene in rGO and rGO/MXene sponge, in their respective microstructures (side view in Fig. 2(f and i)). This integration of VSe_2 nanosheets into the cross-linked 3D microstructure restricts the aggregation of VSe_2 nanosheets exposing the maximum active sites for the electrochemical process. Fig. 2(c) shows a photograph of the 3D VSe_2@G/MXe microstructure on a leaf which confirms its ultralight density due to its pore-rich interior.

In addition, to gain insight into the elemental compositions, the EDX spectra of VSe_2, VSe_2@G, and VSe_2@G/MXe were recorded and are shown in Fig. S1(a–c).† The EDX profiles of all electrocatalysts exhibit signals from V and Se along with other elements, *i.e.*, C, O, and Ti, in the corresponding electrocatalyst. The appearance of peaks from all conforming elements (V, Se, Ti, C, and O) in VSe_2@G/MXe confirms the successful assembly of VSe_2, MXene, and rGO into a 3D microstructure.

3.2. Phase analysis

XRD analysis was carried out to evaluate the phase purity and crystal structure of the synthesized samples. Multiple diffraction peaks of the MXene (Fig. S2†) at 8.4°, 17.8°, 26.7°, 36.1°, 39.7°, and 60.3° can be indexed to the (002), (004), (006), (103), (104), and (110) planes of the $Ti_3C_2T_x$ MXene phase (JCPDS card: 52-0875), respectively.[39] Fig. 3(a) shows the XRD patterns of VSe_2, VSe_2@G and VSe_2@G/MXe. For VSe_2, the peaks observed at 14.6°, 29°, 30.2°, 33.9°, 43.1°, 53.9°, and 54.8° are attributed to the (001), (002), (100), (011), (102), (110), and (103) planes of the hexagonal crystalline phase of VSe_2 (JCPDS: 01-089-1641), respectively.[40] The XRD patterns of VSe_2@G show an additional distinctive broad bump at around 23.9° that corresponds to the (002) plane of rGO (Fig. S2†) in addition to the peaks of VSe_2. This broad bump at 23.9° corresponds well to hydrothermally reduced rGO previously reported in the literature.[41] Likewise, for VSe_2@G/MXe, in addition to VSe_2 and rGO, two new peaks appeared from the (002) and (004) planes of the MXene. Noticeably, the (002) peak of the MXene gets shifted from 8.4° to 7.7° in VSe_2@G/MXe. This shift is presumably related to the expansion in the interlayer spacing of the MXene from 1.05 nm to 1.14 nm, after its incorporation into the rGO based sponge.[42] Furthermore, the absence of any extra peak from impurity confirms the phase purity of the prepared samples.

3.3. Functional group analysis

Different vibrational modes associated with functional groups present in VSe_2, VSe_2@G, and VSe_2@G/MXe were examined by FT-IR analysis, as shown in Fig. 3(b). The FT-IR spectrum of VSe_2 exhibits two IR bands in the fingerprint region at 585 cm^{-1} and 742 cm^{-1} corresponding to different vibrational modes of the V–Se bond.[43] A broad band at around 3461 cm^{-1} is contributed by the symmetric and asymmetric stretching vibrations of the O–H group associated with physically adsorbed water on the surface of VSe_2.[44] In contrast to the spectrum of VSe_2, the FT-IR spectra of VSe_2@G and VSe_2@G/MXe exhibit several new bands in the ~1000–2000 region, corresponding to the functional groups of rGO and the MXene. Bands that appeared at around 1392 cm^{-1} and 1569 cm^{-1} belong to C–H bond bending and C=C bond stretching vibrations from graphitic domains of rGO, respectively.[45] The characteristic bands at 1005 cm^{-1}, 1222 cm^{-1}, and 1685 cm^{-1} are adhered by the oxygen containing functional groups in VSe_2@G and VSe_2@G/MXe microstructures.

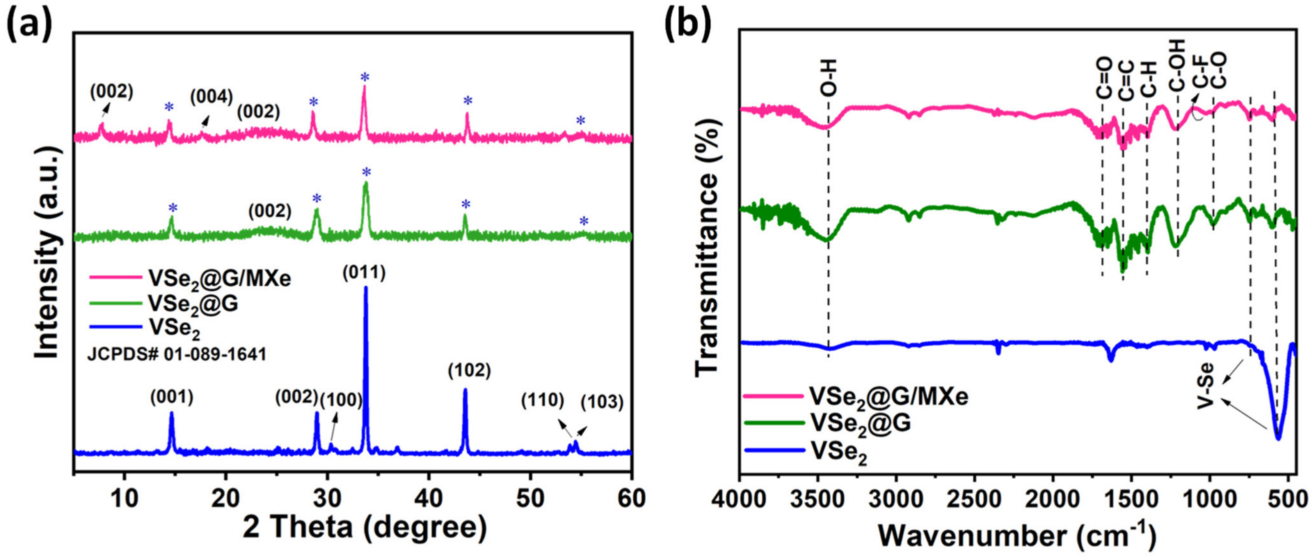

Fig. 3 (a) XRD patterns and (b) FT-IR spectra of VSe_2, VSe_2@G, and VSe_2@G/MXe.

Specifically, bands at 1005 cm^{-1} and 1685 cm^{-1} can be assigned to the stretching modes of C–O and C═O bonds.[46] An intense band identified at 1204 cm^{-1} represents a combined contribution from C–O stretch and O–H deformation vibrations.[47] Additionally, a small band at 1033 cm^{-1} in VSe_2@G/MXe corresponds to the C–F stretch of the HF-etched MXene.[48] Moreover, the considerably deeper O–H bond for VSe_2@G and VSe_2@G/MXe infers the hydrophilic surface characteristic of the prepared electrocatalysts which is also evident from the existence of vibrational modes from different hydrophilic groups (C–O, C═O, O–H, and C–F). These hydrophilic groups are particularly desirable for electrocatalysts as they tend to improve the interaction with electrolyte ions and in turn boost up the electrochemical performance of the electrocatalytic material.[49] In addition, these functional groups on the surface of 3D sponges are involved in interfacial interactions with VSe_2 for enhanced charge transport and stability during the electrochemical operation.[50]

3.4. Physisorption analysis

N_2 adsorption–desorption measurements were performed at 77 K to analyze the surface area and porous characteristics of VSe_2@G and VSe_2@G/MXe microstructures and bare VSe_2. As displayed in Fig. 4(a), all samples exhibited a type-IV adsorption isotherm. Well defined hysteresis loops can be observed in the adsorption–desorption isotherms for VSe_2@G and VSe_2@G/MXe microstructures with no limiting adsorption at a high relative pressure, indicating the characteristic of the H_3-type hysteresis loop.[51] Capillary condensation in porous VSe_2@G and VSe_2@G/MXe microstructures occurred at a relative pressure P/P_o = ∼0.4 which directs to the presence of a large number of mesopores.[52] The BET specific surface area (SSA) for VSe_2 was found to be 15 m^2 g^{-1} which increased to 40.4 and 43.9 m^2 g^{-1} for VSe_2@G and VSe_2@G/MXe, respectively. Apparently, rGO contributes significantly to the enhancement of the SSA. Even though the SSAs of VSe_2@G and VSe_2@G/MXe are comparable, VSe_2@G/MXe showed a higher SSA than that of the previously reported 2D MXene.[53] This implies better surface accessibility of the MXene after its assembly into a 3D microstructure. Fig. 4(b) shows the pore size distribution curves of VSe_2, VSe_2@G, and VSe_2@G/MXe. In contrast to VSe_2, VSe_2@G and VSe_2@G/MXe porous microstructures exhibit wide pore size distribution with mean pore diameters in the mesoporous and macroporous range. The BJH desorption average peak pore diameter for VSe_2@G was found to be 16.33 nm which shifted to 11.18 nm for VSe_2@G/MXe. The result suggests that the addition of the MXene most likely affects the crosslinking ability and density of ice crystals formed during the freeze-drying process, which ultimately affects the textural properties and average pore size of the resulting microstructure.

3.5. Conductivity measurements

The electrical behavior of VSe_2, VSe_2@G, and VSe_2@G/MXe was analyzed by the two-probe current–voltage (*I*–*V*) measurements by converting the samples into a pellet with the help of a hydraulic press. Fig. S3† shows the *I*–*V* profiles of all samples under the applied voltage range of −10 to 10 V. Current responses for all the samples followed Ohm's law with a typical linear relationship between the current and voltage

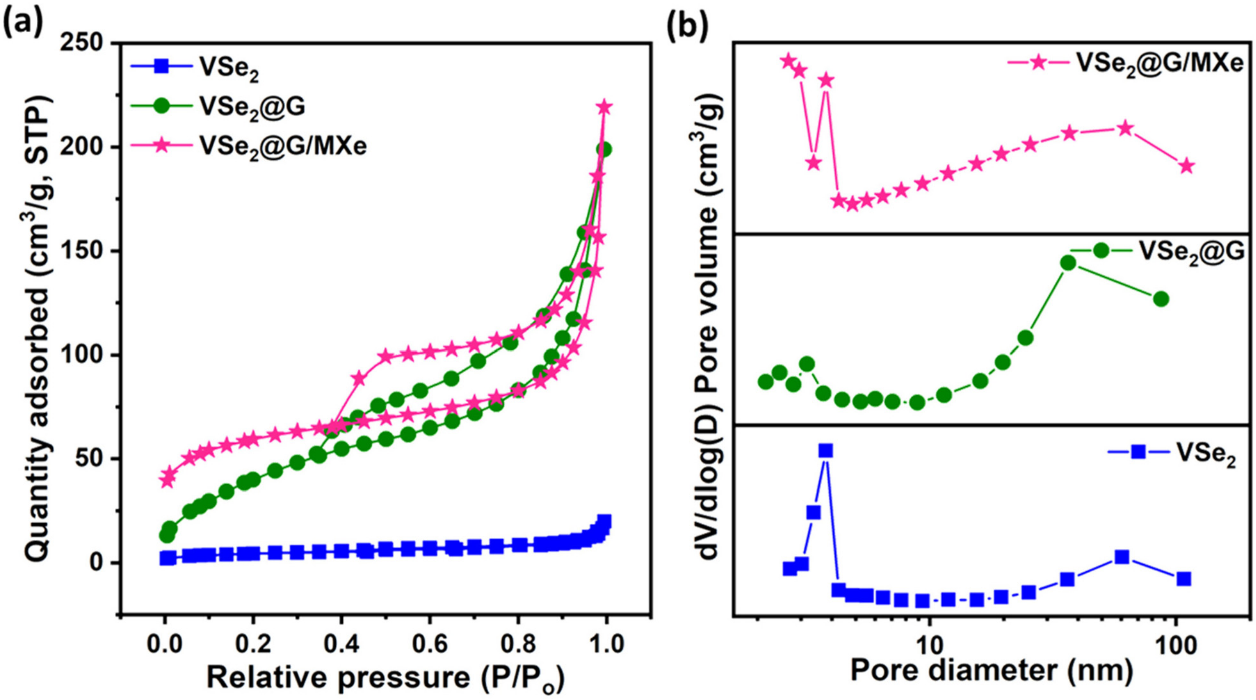

Fig. 4 (a) N_2 adsorption–desorption isotherms and (b) pore size distribution curves of VSe_2, VSe_2@G, and VSe_2@G/MXe.

axes. Evidently, the current response for the electrocatalysts under the same applied voltage was in the order VSe_2@G/MXe > VSe_2@G > VSe_2. This indicates that VSe_2@G/MXe exhibited the lowest electrical resistance and high conductivity among all electrocatalysts. The electrical conductivity (σ) for each electrocatalyst was calculated using eqn (5).

$$\sigma = \frac{w}{R \times A} \tag{5}$$

In the above equation, w and A denote the width and area of the pellet, respectively, and R is the resistance obtained from the slope of the I–V profile. The electrical conductivities of VSe_2, VSe_2@G, and VSe_2@G/MXe were found to be 8.84×10^{-8}, 2.15×10^{-7}, and 5×10^{-7} S cm^{-1}, respectively. The low electrical resistance and significant improvement in the electrical conductivity of VSe_2@G/MXe as compared to VSe_2 and VSe_2@G are reasonably ascribed to the integration of highly conductive MXene sheets into the 3D matrix and generation of ohmic contacts among the individual components of the VSe_2@G/MXe microstructure.[54] The higher electrical conductivity of VSe_2@G/MXe is expected to promote the transport of electrons during the electrochemical activity.

3.6. Water-splitting experiments

To evaluate the overall water-splitting performance, HER and OER catalytic activities of bare VSe_2 and sponge-like VSe_2@G and VSe_2@G/MXe microstructures were analyzed in 1 M KOH as the alkaline medium. Fig. 5(a) exhibits IR-corrected polarization curves for the HER activity measured at 3 mV s^{-1}. For comparison, the HER performance of commercial Pt/C and the NF substrate is also shown. Notably, Pt/C showed the highest HER activity and NF was the least active. The onset potential for the HER in the presence of VSe_2, VSe_2/G, and VSe_2@G/MXe electrocatalysts was observed at −0.19, −0.15, and −0.11 V, respectively. To achieve a cathodic current density of 10 mA cm^{-2}, VSe_2 required an overpotential of 261 mV that decreased significantly for VSe_2@G and VSe_2@G/MXe to 202 and 153 mV, respectively to reach the same current density. This finding suggests that integration of VSe_2 into the 3D rGO and rGO/MXene based sponge is beneficial for the electrochemical activity. Nonetheless, the overpotential for VSe_2@G/MXe is the lowest which signifies its greater HER activity among all electrocatalysts. The LSV curve depicted in Fig. S4† illustrates a discernable HER activity for pure G/MXe (overpotential = 307 mV at 10 mA cm^{-2}) which is anticipated to be contributed by the redox-active Ti^{+3}/Ti^{+4} in the MXene. However, this activity when solely relying on G/MXe is notably lower than that of VSe_2, indicating that the active sites for the HER activity are predominantly contributed by VSe_2. In this way, the enhanced electrocatalytic performance of VSe_2@G/MXe can be explained by its 3D sponge-like structure, rich in mesopores and macropores, coupled with the high electrical conductivity of G/MXe. This structure exposes more active sites of VSe_2 and facilitates rapid ion and electron transport, thereby increasing the active site efficiency of VSe_2@G/MXe during the HER. To comprehend the kinetics of HER activity, Tafel slopes (b) for all electrocatalysts were obtained from the corresponding polarization curves according to the following equation for the half-cell reaction (6):

$$\eta = b \log(j) \tag{6}$$

In the above equation, η denotes the overpotential and j is the current density. As depicted in Fig. 5(b), Tafel slopes for VSe_2, VSe_2@G, and VSe_2@G/MXe are 140, 107, and 84 mV dec^{-1}, respectively. Generally, the HER activity in alkaline media proceeds through the water dissociation Volmer step (*i.e.*, $H_2O + e^- \leftrightarrow H_{ads} + OH^-$) and thereupon by the Heyrovsky step (*i.e.*, $H_2O + H_{ads} \leftrightarrow H_2 + OH^-$) or the Tafel reaction (*i.e.*, $2H_{ads} \leftrightarrow H_2$). The theoretical values of the Tafel slopes for the Volmer, Heyrovsky, and Tafel reactions are 120, 40, and 30 mV dec^{-1}, respectively.[20] For VSe_2@G/MXe, a value of 84 mV dec^{-1} for the Tafel slope indicates a typical Volmer–Heyrovsky mechanism, where electrochemical desorption or the Heyrovsky reaction is the rate-limiting step.[55] For Tafel slopes close to 120 mV dec^{-1}, primary water dissociation (the Volmer reaction) is the rate limiting step, suggesting different H_2 evolution kinetics for VSe_2 and VSe_2@G from that of VSe_2@G/MXe. Clearly, a small value of Tafel slope for VSe_2@G/MXe demonstrates better kinetics for H_2 evolution in the presence of the VSe_2@G/MXe electrocatalyst.

Furthermore, considering the current density and concentration of V ions, the turnover frequency (TOF) was determined for all electrocatalysts at different overpotentials, as shown in Fig. 5(c). For bare VSe_2, the TOF can reach up to 0.027 s^{-1} at 0.3 V, which elevated to 0.093 s^{-1} for VSe_2@G and was the maximum, *i.e.*, 0.15 s^{-1}, in the presence of VSe_2@G/MXe. However, the calculated value of the TOF can be the upper hold as not all the V ions are necessarily accessible for catalytic activity. Nonetheless, the least overpotential and Tafel slope for VSe_2@G/MXe are convincing for its highest TOF value and it must have provided the maximum number of active sites and accessibility of electrolyte to the active sites for the significant HER activity.[56]

The low overpotential (153 mV), Tafel slope (84 mV dec^{-1}), and high TOF (0.15 s^{-1}) for VSe_2@G/MXe can be ascribed to its enhanced intrinsic characteristics. In addition to the 3D spongy framework, the hydrophilicity of VSe_2@G/MXe combined with its high electrical conductivity improves the electrical contact of reactants to the active sites of VSe_2@G/MXe and hence in succession tailors the free energy for H-adsorption through the synergistic effects of VSe_2 and the compositing material (G/MXe).[57]

Moreover, electrochemical impedance measurements were performed to analyze the charge transfer kinetics during the electrochemical reaction. The corresponding Nyquist plots (Re(Z) *vs.* −Im(Z)) derived from the impedance data show a characteristic Nyquist arc along the real impedance axis for all the prepared electrocatalysts (Fig. 5(d)). The equivalent fitted circuit (Randle's circuit) for Nyquist was used to determine the charge transfer resistance (R_{ct}). Obviously, VSe_2@G/MXe shows a smaller Nyquist arc with a low R_{ct} of 9.1 Ω that is far less

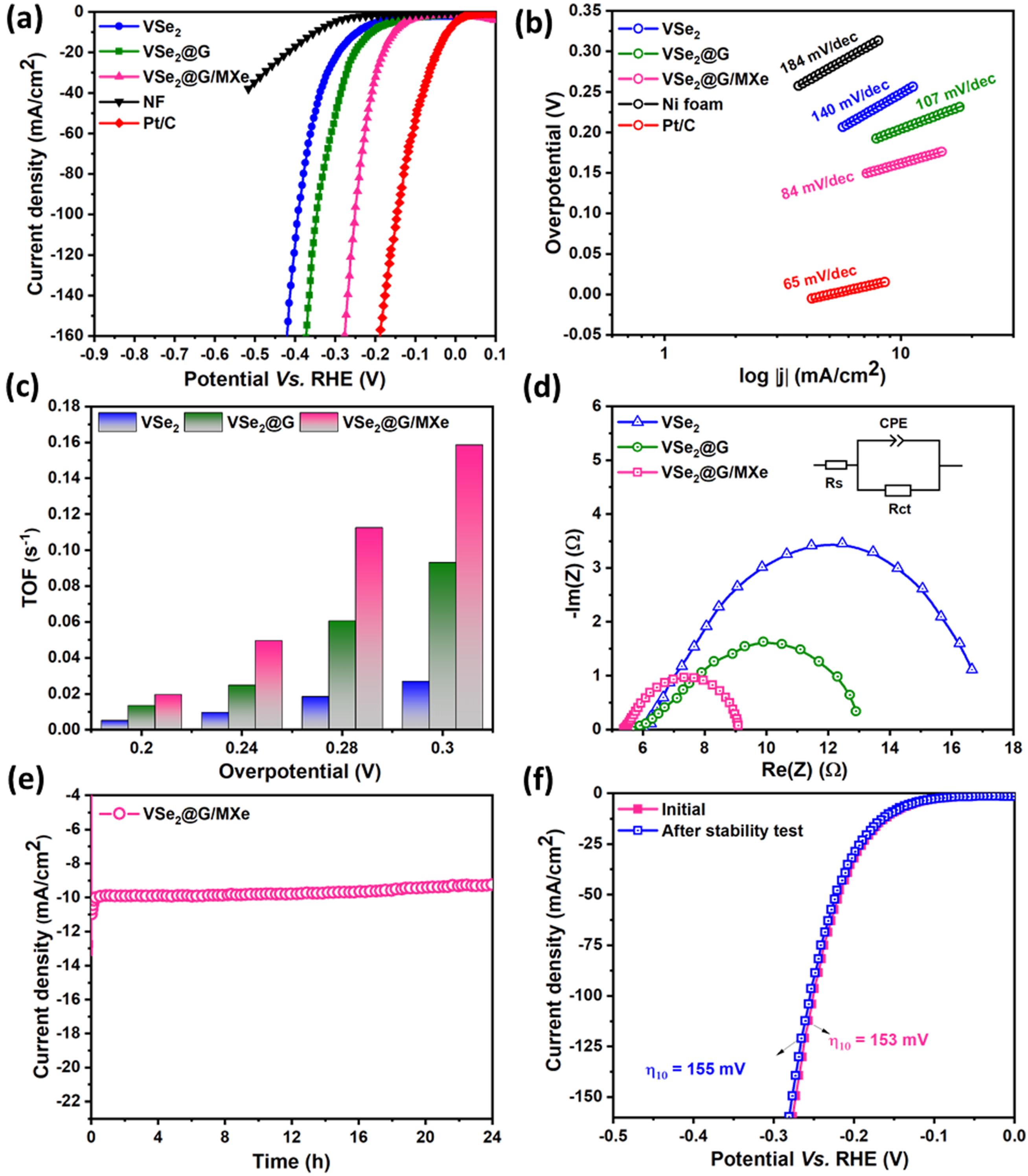

Fig. 5 Electrochemical measurements for the HER activity in 1 M KOH of VSe_2, VSe_2@G, and VSe_2@G/MXe: (a) LSV curves measured at 3 mV s^{-1}, (b) Tafel plots, (c) TOF at 0.2, 0.24, 0.28, and 0.3 V, (d) Nyquist plots at 0.1 Hz to 100 kHz, (e) chronoamperometry test of VSe_2@G/MXe for 24 h, and (f) LSV tests of VSe_2@G/MXe for 1000 cycles at 100 mV s^{-1}.

than those of VSe_2@G (12.8 Ω) and VSe_2 (16.5 Ω), indicating a low resistance to charge transfer on the surface of VSe_2@G/MXe than those of the counterpart electrocatalysts.

Besides the catalytic performance, stability is also an important parameter to assess the potential practical application of an electrocatalyst. The stability of VSe_2@G/MXe was evaluated through the chronoamperometric and LSV measurements. The chronoamperometry results, displayed in Fig. 5(e), show that at a constant overpotential, the current density fluctuates with a very small loss after a long period of 24 h. This small fluctuation in the current density can possibly be caused by the hydronium consumption or lingering H_2 bubbles that impede the HER activity, as also previously reported by Zhu *et al.*[20] Alternatively, LSV tests were conducted at a high scan rate of 100 mV s^{-1} for 1000 cycles to further confirm the stability of VSe_2@G/MXe. As shown in Fig. 5(f), the VSe_2@G/MXe electrocatalyst maintains the initial overpotential with a slight shift from 153 mV to 155 mV over continuous 1000 LSV scans.

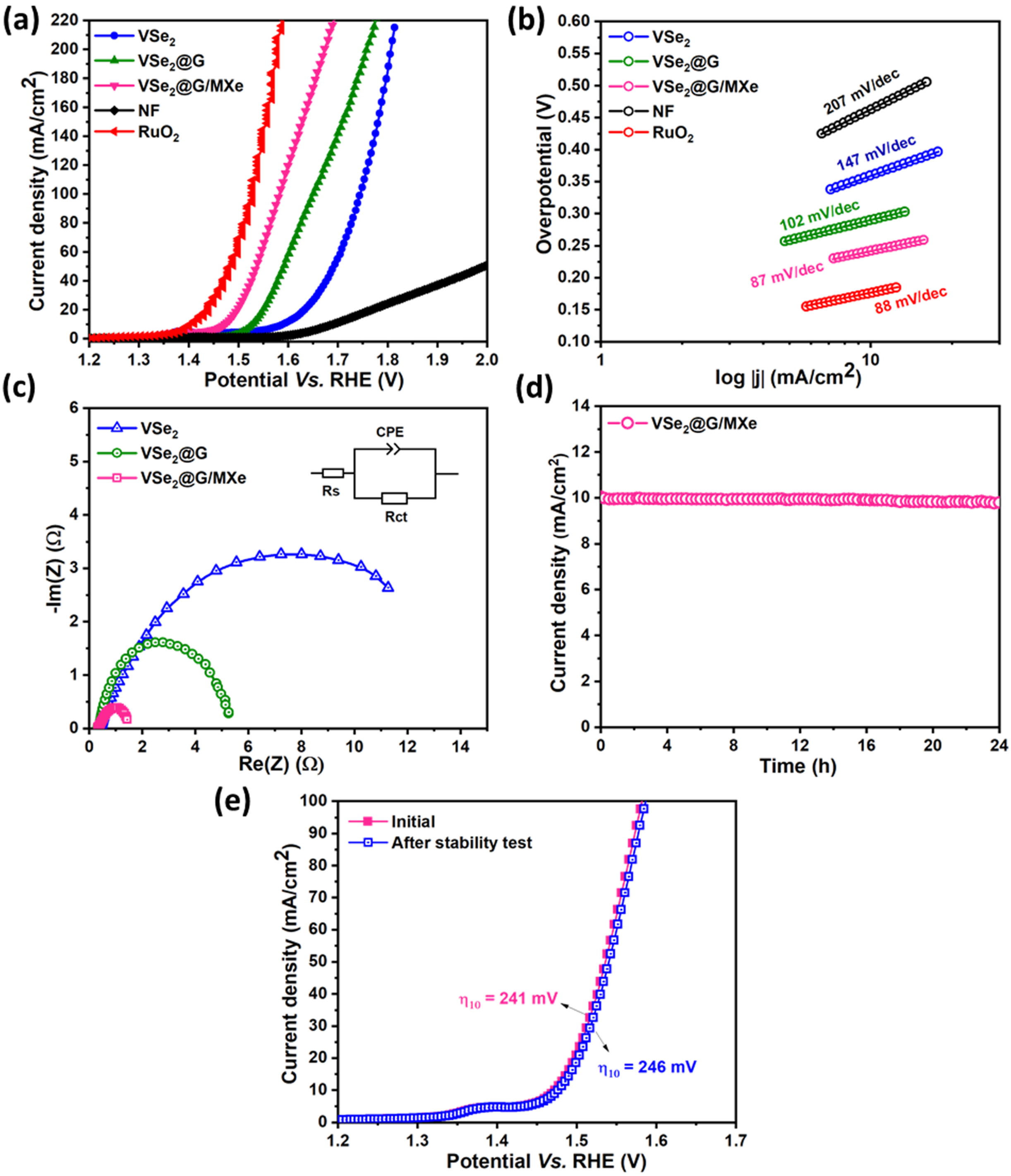

Fig. 6 Electrochemical measurements for the OER activity in 1 M KOH of VSe_2, VSe_2@G, and VSe_2@G/MXe: (a) LSV curves measured at 3 mV s^{-1}, (b) Tafel plots, (c) Nyquist plots at 0.1 Hz to 100 kHz, (d) chronoamperometry test of VSe_2@G/MXe for 24 h, and (e) LSV tests of VSe_2@G/MXe for 1000 cycles at 100 mV s^{-1}.

These results confirm the mechanical robustness and chemical durability of the VSe_2@G/MXe electrocatalyst. This enhanced stability of VSe_2@G/MXe can be anticipated to be contributed by the integration of VSe_2 into G/MXe which (i) prevents the aggregation of VSe_2 sheets and (ii) provides better dispersion of active sites, thus minimizing the mechanical stress concentrations. Additionally, as mentioned beforehand, the interfacial interactions between G/MXe and VSe_2 impede the percolation of VSe_2 sheets during the electrocatalytic activity.

Driven by the promising HER performance, the catalytic activities of the prepared electrocatalysts for the OER were also evaluated in 1 M KOH within the same electrochemical setup. Fig. 6(a) and Fig. S5† show IR-corrected polarization curves for the OER in the presence of the NF substrate, VSe_2, VSe_2@G, VSe_2@G/MXe, benchmark RuO_2 and G/MXe, respectively. Similar to the HER, commercial RuO_2 showed the highest activity while the NF substrate and G/MXe exhibited the lowest activity for the OER. The onset potentials for VSe_2, VSe_2@G, and VSe_2@G/MXe were recorded at 0.34, 0.23, and 0.19 V, respectively. Obviously, VSe_2@G/MXe offered an earlier onset of the anodic current as compared to its analogs after the benchmark RuO_2. Following this, VSe_2@G/MXe also outperformed other electrocatalysts in terms of the overpotential for the OER with an optimum potential of 241 mV to drive an anodic current density of 10 mA cm^{-2}. The overpotentials for G/MXe, VSe_2, and VSe_2@G to drive the same current density were found to be 419, 347, and 293 mV, respectively. To compare the OER kinetics, the Tafel slope of each electrocatalyst was obtained from the corresponding polarization curve, as shown in Fig. 6(b). Tafel slopes for VSe_2, VSe_2@G and VSe_2@G/MXe were 147, 102, and 87 mV dec^{-1}. Notably, the

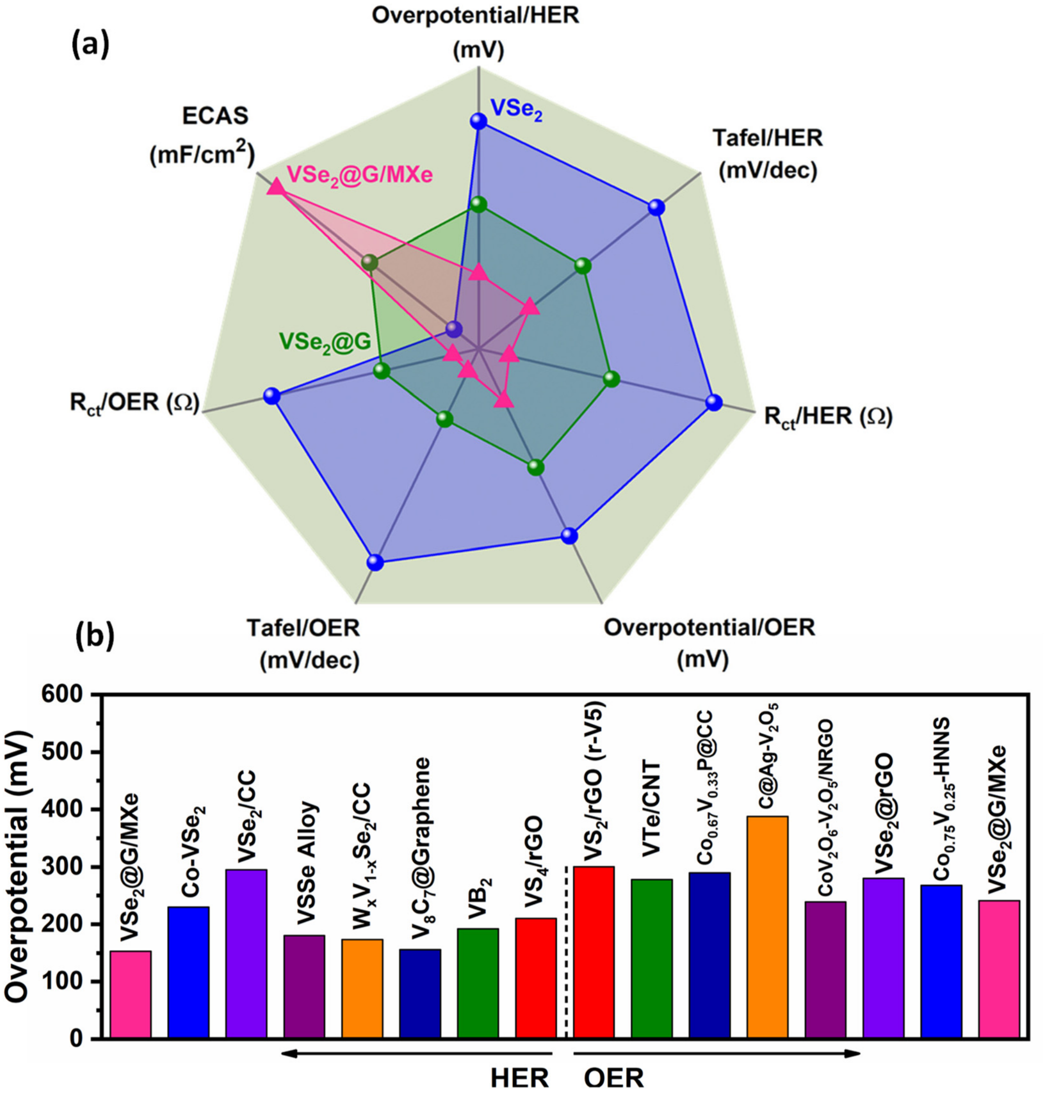

Fig. 7 (a) Radar plot showing a comparison of different electrochemical parameters obtained for VSe_2, VSe_2@G, and VSe_2@G/MXe from the HER and OER activity and (b) bar graph showing a comparison of the performance of VSe_2@G/MXe for the HER and OER activities in terms of overpotential with that of similar reported electrocatalytic materials.

Tafel slope of VSe_2@G/MXe approaches the Tafel slope of benchmark RuO_2. It is well reported that the OER mechanism embraces multiple steps of electron/proton transfer reactions. The value of the Tafel slope for the OER (87 mV) in the presence of VSe_2@G/MXe suggests that the rate-limiting step should be toward the end of the O_2 evolution process as $MOOH + HO^- \rightarrow MOO^- + H_2O$, where M represents a site on the surface of the electrocatalyst.[58] Meanwhile, impedance measurement in Fig. 6(c) shows R_{ct} values in descending order as we proceed from VSe_2 (11.2 Ω), VSe_2@G (5.25 Ω), and VSe_2@G/MXe (1.41 Ω). As previously observed for the HER, a considerably small diameter of a Nyquist arc and a small value of the R_{ct} indicate an enhanced electron transfer across the electrode–electrolyte interface at VSe_2@G/MXe. Chronoamperometric measurements at a constant overpotential (Fig. 6(d)) show that VSe_2@G/MXe maintains an almost steady current output for 24 h with a small loss in current density. Likewise, LSV measurements in Fig. 6(e) at 100 mV s^{-1} for continuous 1000 LSV cycles resulted in a small overpotential shift from 241 mV to 246 mV, which confirms the durability of VSe_2@G/MXe for the OER activity.

To get a deeper understanding of the intrinsic electrochemical activity of VSe_2@G/MXe, the electrochemical double layer capacitance (C_{dl}) was determined for all the electrocatalysts from the CV measurements at different scan rates (20–120 mV s^{-1}). Fig. S6† displays CV curves for VSe_2, VSe_2@G, and VSe_2@G/MXe recorded within a voltage range of 0.4–0.5 V where the output current is believed to be contributed by the electrical double layer charging. Linear plots of scan rate *vs.* anodic and cathodic current densities were fitted to obtain the C_{dl} value. The average C_{dl} values for VSe_2, VSe_2@G, and VSe_2@G/MXe were found to be 5.1, 8.9, and 13.1 mF cm^{-2}. C_{dl} is usually considered to be proportional to the electrochemical active surface area (ECAS) of the electrode–electrolyte interface for charge transfer during the electrochemical reaction.[59] A high C_{dl} or ECAS of VSe_2@G/MXe is due to the synergistic combination of VSe_2 and G/MXe that engenders an architecture that optimally exposes VSe_2 active sites while concurrently promoting efficient charge transfer, subsequently enhancing the available electroactive surface area for electrocatalytic activity.

Moreover, the ECAS-normalized current density displayed in Fig. S7 and S8† shows a higher current density of VSe_2@G/MXe than that of VSe_2 for both the HER and OER, as is also observed in the case of geometric surface area–normalized current density. This approves the superior intrinsic electrocatalytic activity of VSe_2@G/MXe for the HER and the OER.

Fig. 7(a) shows a radar plot comparing different electrochemical parameters (overpotential, Tafel slope, ECAS, and R_{ct}) obtained from water-splitting measurements. For both the HER and OER, the electrocatalytic activity of VSe_2@G/MXe was significant as compared to those of VSe_2@G and VSe_2. Moreover, the HER and OER activities of VSe_2@G/MXe were also comparable or even better than previously reported similar electrocatalysts (Fig. 7(b) and Tables S1 and S2†).

The superior electrochemical performance of VSe_2@G/MXe can be accredited to its large SSA, large number of exposed electroactive sites, hydrophilicity, and high conductivity of G/MXe. These characteristics of VSe_2@G/MXe are the outcomes

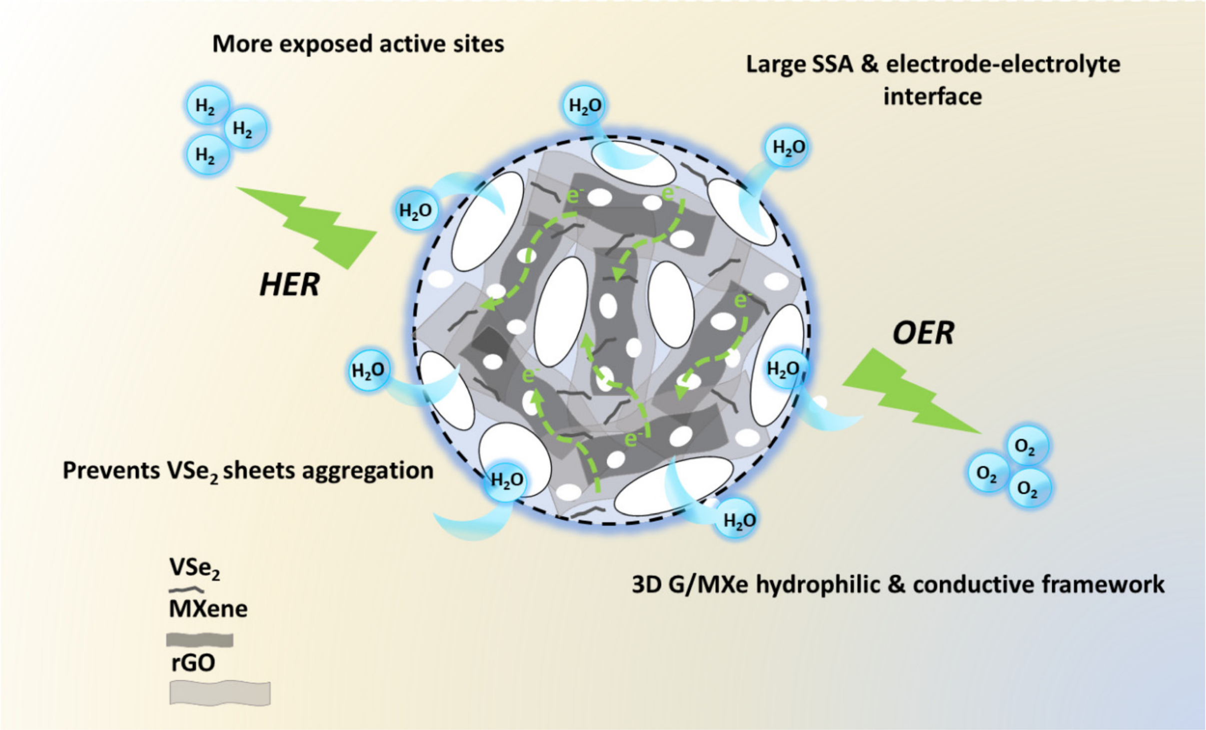

Fig. 8 Schematic diagram of structural and componential attributes of VSe_2@G/MXe for boosted overall water-splitting performance.

that resulted from the individual components (VSe_2, rGO, and MXene) and their synergistic effects, and most importantly from the morphological engineering of VSe_2@G/MXe into the 3D sponge like framework (Fig. 8).

4. Conclusions

In summary, an effective strategy was used to assemble VSe_2 into a MXene/rGO matrix-based 3D microstructure as VSe_2@G/MXe. Physiochemical characterization of VSe_2@G/MXe exhibited a sponge-like pore-rich skeleton for VSe_2@G/MXe with a high SSA of 43.9 $m^2\ g^{-1}$ and an electrical conductivity of 5×10^{-7} S cm^{-1}. Assembly of VSe_2 in a 3D sponge prevented the aggregation of VSe_2 nanosheets, thereby exposing maximum active sites for the electrochemical reaction. Intrinsic characteristics of individual components (VSe_2, MXene, and rGO) and the unique morphology of VSe_2@G/MXe synergistically worked together to improve the inherent electrocatalytic activity of the VSe_2@G/MXe microstructure. As a bifunctional electrocatalyst, VSe_2@G/MXe exhibited significant electrochemical activity with low overpotentials of 153 mV and 241 mV to attain 10 mA cm^{-2}, for the HER and OER activities, respectively. Chronoamperometry and LSV stability tests confirmed the long-term stability of VSe_2@G/MXe. Hence, this work can pave the way to develop high performance 3D electrocatalysts for efficient energy conversion and water-splitting applications.

Conflicts of interest

There are no conflicts to declare.

Acknowledgements

This work was supported by the Distinguished Scientist Fellowship Program (DSFP) at King Saud University, Riyadh, Saudi Arabia. Prof. Dr. Sonia Zulfiqar is highly grateful for the funding provided by the Statutory City of Ostrava, Czechia through the Research Grant "Global Experts" and to the American University in Cairo, Egypt for using STRC instrumental facilities. Profs. Cochran and Zulfiqar are grateful to the National Science Foundation for the financial support through research grants NSF-2113695, NSF-2242763 and NSF-2218070.

References

1 M. Mersch, C. N. Markides and N. Mac Dowell, The impact of the energy crisis on the UK's net-zero transition, *iScience*, 2023, **26**, 106491.

2 B.-B. Sui, L. Sha, P.-F. Wang, Z. Gong, Y.-H. Zhang, Y.-H. Wu, L.-N. Zhao, J.-J. Tang and F.-N. Shi, In situ zinc citrate on the surface of Zn anode improves the performance of aqueous zinc-ion batteries, *J. Energy Storage*, 2024, **82**, 110550.

3 S. Wang, Y. Liu, L. He, Y. Sun, Q. Huang, S. Xu, X. Qiu and T. Wei, A Gel Polymer Electrolyte Based on IL@ NH_2-MIL-53 (Al) for High-Performance All-Solid-State Lithium Metal Batteries, *Chin. J. Chem. Eng.*, 2024, DOI: **10.1016/j.cjche.2024.01.017**.

4 F. Adedoyin, I. Ozturk, I. Abubakar, T. Kumeka, O. Folarin and F. V. Bekun, Structural breaks in CO_2 emissions: are they caused by climate change protests or other factors?, *J. Environ. Manage.*, 2020, **266**, 110628.

5 Q. Li, H. Wang, H. Yu, M. Fu, W. Liu, Q. Zhao, S. Huang, L. Zhou, W. Wei and X. Ji, Engineering an Ultrathin and Hydrophobic Composite Zinc Anode with 24 μm Thickness for High–Performance Zn Batteries, *Adv. Funct. Mater.*, 2023, **33**, 2303466.

6 N. Muradov, Low to near-zero CO_2 production of hydrogen from fossil fuels: Status and perspectives, *Int. J. Hydrogen Energy*, 2017, **42**, 14058–14088.

7 Z. Sun, S. Yu, S. Toan, R. Abiev, M. Fan and Z. Sun, Enabling low-temperature methanol activation via lattice oxygen induced Cu–O–Cr catalysis, *ACS Catal.*, 2023, **13**, 13704–13716.

8 G.-F. Chen, Y. Luo, L.-X. Ding and H. Wang, Low-voltage electrolytic hydrogen production derived from efficient water and ethanol oxidation on fluorine-modified FeOOH anode, *ACS Catal.*, 2018, **8**, 526–530.

9 X. Cai, X. Li, J. You, F. Yang, Z. Shadike, S. Qin, L. Luo, Y. Guo, X. Yan and S. Shen, Lithium-mediated ammonia electrosynthesis with ether-based electrolytes, *J. Am. Chem. Soc.*, 2023, **145**, 25716–25725.

10 T. Kato, M. Kubota, N. Kobayashi and Y. Suzuoki, Effective utilization of by-product oxygen from electrolysis hydrogen production, *Energy*, 2005, **30**, 2580–2595.

11 J. Mo, B. I. Stefanov, T. H. Lau, T. Chen, S. Wu, Z. Wang, X.-Q. Gong, I. Wilkinson, G. N. Schmid and S. C. E. Tsang, Superior performance of Ag over Pt for hydrogen evolution reaction in water electrolysis under high overpotentials, *ACS Appl. Energy Mater.*, 2019, **2**, 1221–1228.

12 H. Zhao, Y. Yang, X. Dai, H. Qiao, J. Yong, X. Luan, L. Yu, C. Luan, Y. Wang and X. Zhang, NiCo-DH nanodots anchored on amorphous NiCo-Sulfide sheets as efficient electrocatalysts for oxygen evolution reaction, *Electrochim. Acta*, 2019, **295**, 1085–1092.

13 Y. Liu, J. Cao, Y. Chen, M. Wei, X. Liu, X. Li, Q. Wu, B. Feng, Y. Zhang and L. Yang, Regulation of the morphology and electrochemical properties of $Ni_{0.85}Se$ via Fe doping for overall water splitting and supercapacitors, *CrystEngComm*, 2022, **24**, 1704–1718.

14 W. Li, X. Gao, D. Xiong, F. Wei, W. G. Song, J. Xu and L. Liu, Hydrothermal synthesis of monolithic Co_3Se_4 nanowire electrodes for oxygen evolution and overall water splitting with high efficiency and extraordinary catalytic stability, *Adv. Energy Mater.*, 2017, **7**, 1602579.

15 M. Ahmad, B. Xi, Y. Gu, H. Zhang and S. Xiong, $NiSe_2$/$FeSe_2$ heterostructured nanoparticles supported on rGO for

efficient water electrolysis, *Inorg. Chem. Front.*, 2022, **9**, 448–457.
16 Y. Yin, Y. Zhang, T. Gao, T. Yao, X. Zhang, J. Han, X. Wang, Z. Zhang, P. Xu and P. Zhang, Synergistic phase and disorder engineering in 1T–$MoSe_2$ nanosheets for enhanced hydrogen–evolution reaction, *Adv. Mater.*, 2017, **29**, 1700311.
17 J. Masud, W. P. Liyanage, X. Cao, A. Saxena and M. Nath, Copper selenides as high-efficiency electrocatalysts for oxygen evolution reaction, *ACS Appl. Energy Mater.*, 2018, **1**, 4075–4083.
18 J. Sun, Z. Zhao, J. Li, Z. Li and X. Meng, Recent advances in transition metal selenides-based electrocatalysts: Rational design and applications in water splitting, *J. Alloys Compd.*, 2022, **918**, 165719.
19 X. Xia, L. Wang, N. Sui, V. L. Colvin and W. Y. William, Recent progress in transition metal selenide electrocatalysts for water splitting, *Nanoscale*, 2020, **12**, 12249–12262.
20 Q. Zhu, M. Shao, S. H. Yu, X. Wang, Z. Tang, B. Chen, H. Cheng, Z. Lu, D. Chua and H. Pan, One-pot synthesis of Co-doped VSe_2 nanosheets for enhanced hydrogen evolution reaction, *ACS Appl. Energy Mater.*, 2018, **2**, 644–653.
21 M. Chhowalla, H. S. Shin, G. Eda, L.-J. Li, K. P. Loh and H. Zhang, The chemistry of two-dimensional layered transition metal dichalcogenide nanosheets, *Nat. Chem.*, 2013, **5**, 263–275.
22 T. G. Ulusoy Ghobadi, B. Patil, F. Karadas, A. K. Okyay and E. Yilmaz, Catalytic properties of vanadium diselenide: a comprehensive study on its electrocatalytic performance in alkaline, neutral, and acidic media, *ACS Omega*, 2017, **2**, 8319–8329.
23 W. Zhao, B. Dong, Z. Guo, G. Su, R. Gao, W. Wang and L. Cao, Colloidal synthesis of VSe_2 single-layer nanosheets as novel electrocatalysts for the hydrogen evolution reaction, *Chem. Commun.*, 2016, **52**, 9228–9231.
24 M. Yan, X. Pan, P. Wang, F. Chen, L. He, G. Jiang, J. Wang, J. Z. Liu, X. Xu and X. Liao, Field-effect tuned adsorption dynamics of VSe_2 nanosheets for enhanced hydrogen evolution reaction, *Nano Lett.*, 2017, **17**, 4109–4115.
25 S. Liu, S. Liu, Z. Huang, Y. Liu and X. Qi, 2D vanadium diselenide as a high performance catalyst, *Mater. Sci. Eng., B*, 2020, **260**, 114619.
26 T. D. Thanh, N. D. Chuong, H. Van Hien, T. Kshetri, N. H. Kim and J. H. Lee, Recent advances in two-dimensional transition metal dichalcogenides-graphene heterostructured materials for electrochemical applications, *Prog. Mater. Sci.*, 2018, **96**, 51–85.
27 H. Ren, L. Yu, L. Yang, Z.-H. Huang, F. Kang and R. Lv, Efficient electrocatalytic overall water splitting and structural evolution of cobalt iron selenide by one-step electrodeposition, *J. Energy Chem.*, 2021, **60**, 194–201.
28 X. Zhao, B. Fan, N. Qiao, R. A. Soomro, R. Zhang and B. Xu, Stabilized $Ti_3C_2T_x$-doped 3D vesicle polypyrrole coating for efficient protection toward copper in artificial seawater, *Appl. Surf. Sci.*, 2024, **642**, 158639.
29 T. Kshetri, D. T. Tran, H. T. Le, D. C. Nguyen, H. Van Hoa, N. H. Kim and J. H. Lee, Recent advances in MXene-based nanocomposites for electrochemical energy storage applications, *Prog. Mater. Sci.*, 2021, **117**, 100733.
30 P. K. L. Tran, M. S. Kim, T. H. Nguyen, D. T. Tran, N. H. Kim and J. H. Lee, Interfacial engineering for design of novel 2D cobalt sulfide-Mxene heterostructured catalyst toward alkaline water splitting, *Funct. Compos. Struct.*, 2021, **3**, 045005.
31 Y. Xie, H. Yu, L. Deng, R. Amin, D. Yu, A. E. Fetohi, M. Y. Maximov, L. Li, K. El-Khatib and S. Peng, Anchoring stable FeS_2 nanoparticles on MXene nanosheets via interface engineering for efficient water splitting, *Inorg. Chem. Front.*, 2022, **9**, 662–669.
32 B. Sarfraz, M. T. Mehran, F. Shahzad, S. Hussain, S. R. Naqvi, H. A. Khan and K. Mahmood, Bifunctional CuS/Cl-terminated greener MXene electrocatalyst for efficient hydrogen production by water splitting, *RSC Adv.*, 2023, **13**, 22017–22028.
33 L. Hong, S. Ju, Y. Yang, J. Zheng, G. Xia, Z. Huang, X. Liu and X. Yu, Hollow-shell structured porous $CoSe_2$ microspheres encapsulated by MXene nanosheets for advanced lithium storage, *Sustainable Energy Fuels*, 2020, **4**, 2352–2362.
34 Y. Liu, J. Gong, J. Wang, C. Hu, M. Xie, X. Jin, S. Wang and Y. Dai, Facile fabrication of MXene supported nickel-cobalt selenide ternary composite via one-step hydrothermal for high-performance asymmetric supercapacitors, *J. Alloys Compd.*, 2022, **899**, 163354.
35 Y. Liu, J. Yu, D. Guo, Z. Li and Y. Su, $Ti_3C_2T_x$ MXene/graphene nanocomposites: Synthesis and application in electrochemical energy storage, *J. Alloys Compd.*, 2020, **815**, 152403.
36 C. Zhu, Y. Hao, H. Wu, M. Chen, B. Quan, S. Liu, X. Hu, S. Liu, Q. Ji and X. Lu, Self-Assembly of Binderless MXene Aerogel for Multiple-Scenario and Responsive Phase Change Composites with Ultrahigh Thermal Energy Storage Density and Exceptional Electromagnetic Interference Shielding, *Nano-Micro Lett.*, 2024, **16**, 57.
37 K. Chaudhary, N. Shaheen, S. Zulfiqar, M. I. Sarwar, M. Suleman, P. O. Agboola, I. Shakir and M. F. Warsi, Binary WO_3-ZnO nanostructures supported rGO ternary nanocomposite for visible light driven photocatalytic degradation of methylene blue, *Synth. Met.*, 2020, **269**, 116526.
38 K. Chaudhary, S. Zulfiqar, H. Somaily, M. Aadil, M. F. Warsi and M. Shahid, Rationally designed multifunctional Ti_3C_2 MXene@Graphene composite aerogel integrated with bimetallic selenides for enhanced supercapacitor performance and overall water splitting, *Electrochim. Acta*, 2022, **431**, 141103.
39 K. Chen, K. Yan, Q. Xie, H. Zhu, X. Li, Z. Dong, G. Yuan, J. Zhang and Y. Cong, MXene-derived C-doped TiO_2/Ti_3C_2 heterojunction as a high-performance visible-light photocatalyst, *Res. Chem. Intermed.*, 2022, **48**, 4443–4458.
40 K. Xu, P. Chen, X. Li, C. Wu, Y. Guo, J. Zhao, X. Wu and Y. Xie, Ultrathin nanosheets of vanadium diselenide: a metallic two–dimensional material with ferromagnetic

charge–density–wave behavior, *Angew. Chem.*, 2013, **125**, 10671–10675.

41 H. Liu, B. Sun, P. Zhu, C. Liu, G. Zhang, D. Wang, X. Song, J. Shi, Y. Yang and J. Lu, Preparation of Three–Dimensional Porous Graphene by Hydrothermal and Chemical Reduction with Ascorbic Acid and its Electrochemical Properties, *ChemistryOpen*, 2022, **11**, e202200161.

42 P. Dutta, A. Sikdar, A. Majumdar, M. Borah, N. Padma, S. Ghosh and U. N. Maiti, Graphene aided gelation of MXene with oxidation protected surface for supercapacitor electrodes with excellent gravimetric performance, *Carbon*, 2020, **169**, 225–234.

43 A. K. Singh, N. Shukla, D. K. Verma, B. Kumar, K. Mandal and R. B. Rastogi, Reinforcement of nanoporous lanthanum-doped zinc borate by vanadium selenide nanosheets for improved tribological activity, *RSC Adv.*, 2022, **12**, 18685–18696.

44 L. Mercantili, F. Davis and S. P. Higson, Ultrasonic initiation of the alkaline hydrolysis of triglycerides (saponification) without phase catalysis, *J. Surfactants Deterg.*, 2014, **17**, 133–141.

45 B. C. Ozkan, T. Soganci, H. Turhan and M. Ak, Investigation of rGO and chitosan effects on optical and electrical properties of the conductive polymers for advanced applications, *Electrochim. Acta*, 2019, **295**, 1044–1051.

46 B. Bi, Y. Guan, D. Qiao, X. Chen, M. Bao, Z. Wang and Y. Li, MXene/Graphene modified cellulose aerogel for photo-electro-assisted all-weather cleanup of high-viscous crude oil from spill, *J. Hazard. Mater.*, 2023, **460**, 132353.

47 A. Gholizadeh, A. Malekzadeh and F. Pourarian, Rapid and efficient synthesis of reduced graphene oxide nano-sheets using CO ambient atmosphere as a reducing agent, *J. Mater. Sci.: Mater. Electron.*, 2018, **29**, 19402–19412.

48 B. Scheibe, K. Tadyszak, M. Jarek, N. Michalak, M. Kempiński, M. Lewandowski, B. Peplińska and K. Chybczyńska, Study on the magnetic properties of differently functionalized multilayered $Ti_3C_2T_x$ MXenes and Ti-Al-C carbides, *Appl. Surf. Sci.*, 2019, **479**, 216–224.

49 S. Chen, M. Shi, Q. Xu, J. Xu, X. Duan, Y. Gao, L. Lu, F. Gao, X. Wang and Y. Yu, $Ti_3C_2T_x$ MXene/nitrogen-doped reduced graphene oxide composite: a high-performance electrochemical sensing platform for adrenaline detection, *Nanotechnology*, 2021, **32**, 265501.

50 K. Chaudhary, B. Basha, S. Zulfiqar, S. Yousaf, E. W. Cochran, M. Al-Buriahi, M. F. Warsi and M. Shahid, 3D cellular lattice like-Ti_3C_2 MXene based aerogels embedded with metal selenides particles for energy storage and water splitting applications, *Fuel*, 2023, **351**, 128856.

51 Y. Zhang, K. Li and J. Liao, Facile synthesis of reduced-graphene-oxide/rare-earth-metal-oxide aerogels as a highly efficient adsorbent for Rhodamine-B, *Appl. Surf. Sci.*, 2020, **504**, 144377.

52 M. Lv, W. Xie, S. Sun, G. Wu, L. Zheng, S. Chu, C. Gao and J. Bao, Activated-carbon-supported K–Co–Mo catalysts for synthesis of higher alcohols from syngas, *Catal. Sci. Technol.*, 2015, **5**, 2925–2934.

53 M. Li, R. Sun, Y. Li, J. Jiang, W. Xu, H. Cong and S. Han, The 3D porous "celosia" heterogeneous interface engineering of layered double hydroxide and P-doped molybdenum oxide on MXene promotes overall water-splitting, *Chem. Eng. J.*, 2022, **431**, 133941.

54 L. Huang, X. Deng, S. Pan and W. Cui, Modulating the Schottky barrier of MXenes/2D SiC contacts via functional groups and biaxial strain: a first-principles study, *Phys. Chem. Chem. Phys.*, 2022, **24**, 20837–20847.

55 J. Huang, J. Han, T. Wu, K. Feng, T. Yao, X. Wang, S. Liu, J. Zhong, Z. Zhang and Y. Zhang, Boosting hydrogen transfer during volmer reaction at oxides/metal nanocomposites for efficient alkaline hydrogen evolution, *ACS Energy Lett.*, 2019, **4**, 3002–3010.

56 N. Akbari and M. M. Najafpour, Decoding natural strategy: Oxygen-evolution reaction on the surface of nickel oxyhydroxide at extremely low overpotential, *Inorg. Chem.*, 2023, **62**, 19107–19114.

57 Y. Cheng, Y. Zhang, Y. Li, J. Dai and Y. Song, Hierarchical Ni_2P/Cr_2CT_x (MXene) composites with oxidized surface groups as efficient bifunctional electrocatalysts for overall water splitting, *J. Mater. Chem. A*, 2019, **7**, 9324–9334.

58 T. Shinagawa, A. T. Garcia-Esparza and K. Takanabe, Insight on Tafel slopes from a microkinetic analysis of aqueous electrocatalysis for energy conversion, *Sci. Rep.*, 2015, **5**, 13801.

59 H. Zhang, B. Yang, X. Wu, Z. Li, L. Lei and X. Zhang, Polymorphic $CoSe_2$ with mixed orthorhombic and cubic phases for highly efficient hydrogen evolution reaction, *ACS Appl. Mater. Interfaces*, 2015, **7**, 1772–1779.